Dissecting the conformational complexity and flipping mechanism of bacterial heme transport.

Di Wu[1], Ahmad R Mehdipour[2,3], Franziska Finke[1], Hojjat G Goojani[4], Roan R Groh[1], Tamara N Grund[1], Thomas MB Reichhart[1], Rita Zimmermann[1], Sonja Welsch[5], Dirk Bald[4], Mark Shepherd[6], Gerhard Hummer[2,7], Schara Safarian[1,8,9*]

Affiliations

[1] *Department of Molecular Membrane Biology, Max Planck Institute of Biophysics, D-60438 Frankfurt/Main, Germany*

[2] *Department of Theoretical Biophysics, Max Planck Institute of Biophysics, D-60438 Frankfurt/Main, Germany.*

[3] *Center for Molecular Modeling (CMM), Ghent University, Technologiepark 46, Zwijnaarde, 9052 Belgium.*

[4] *Amsterdam Institute for Life and Environment (A-LIFE), AIMMS, Faculty of Science, Vrije Universiteit Amsterdam, 1081 HZ, Amsterdam, The Netherlands*

[5] *Central Electron Microscopy Facility, Max Planck Institute of Biophysics, D-60438 Frankfurt am Main, Germany*

[6] *School of Biosciences, University of Kent, Canterbury CT2 7NJ, United Kingdom*

[7] *Institute of Biophysics, Goethe University Frankfurt, D-60438 Frankfurt/Main, Germany*

[8] *Department of Microbiology and Immunology, School of Biomedical Sciences, University of Otago, Dunedin, NZ-9054, New Zealand.*

[9] *present address: Fraunhofer Institute for Translational Medicine and Pharmacology ITMP Frankfurt, D-60438 Frankfurt/Main, Germany*

[*]Correspondence and requests for materials should be addressed to Schara Safarian (schara.safarian@biophys.mpg.de).

Abstract

Iron-bound cyclic tetrapyrroles (hemes) are key redox-active cofactors in membrane-integrated oxygen reductases and other bioenergetic enzymes (*1*, *2*). However, the mechanisms of heme transport and insertion into respiratory chain complexes remain unclear. Here we used a combination of cellular, biochemical, structural and computational methods to resolve ongoing controversies around the function of the heterodimeric bacterial ABC transporter CydDC (*3*). We provide multi-level evidence that CydDC is a highly specific heme transporter required for assembly and maturation of cytochrome *bd*, a pharmaceutically relevant drug target. Our systematic single-particle cryo-EM approach combined with atomistic molecular dynamics simulations provides detailed insight into the conformational landscape of CydDC during substrate binding and translocation. We found that heme binds laterally from the membrane space to the transmembrane region of CydDC, enabled by a highly asymmetrical inward-facing CydDC conformation. During the binding process, heme propionates interact with positively charged residues on the surface and later in the substrate-binding pocket of the transporter, causing the heme orientation to flip 180 degree. The membrane-accessible heme entry site of CydDC is primarily controlled by the conformational plasticity of CydD transmembrane helix 4, the extended cytoplasmic segment of which also couples heme confinement to a rotational movement of the CydC nucleotide-binding domain. Our cryo-EM data highlight that this signal transduction mechanism is necessary to drive conformational transitions toward occluded and outward open states.

Introduction

Iron is the second most abundant metal on our planet and an essential trace element for all domains of life (*1*, *2*, *4-7*). It is involved in a multitude of physiological processes such as photosynthesis, protein biosynthesis, nitrogen fixation, nucleic acid repair, and respiration. Cellular iron is found in form of iron-sulfur clusters (Fe-S), iron-bound cyclic tetrapyrroles (hemes), or in its free ionic forms. In biological systems, iron mediates electron transfer by acting as electron acceptor or donor in various biochemical reactions (*8*). Terminal respiratory oxidases such as the mitochondrial cytochrome *c* oxidase and the bacterial cytochrome *bd* oxidase are metalloproteins that rely on their redox active heme cofactors for reduction of molecular oxygen to water (*9-15*). Knowledge about the mechanism of maturation and heme insertion of cytochrome *bd*-type oxidases remains unknown but is urgently required for the development of antimicrobial drugs that can specifically target the energy metabolism and respiratory re-wiring of human pathogenic bacteria upon infection and proliferation (*16*, *17*).

The ABC transporter CydDC is conserved in most bacteria and plays a central role in the biogenesis of membrane-integrated and soluble cytochromes, particularly the insertion of heme into cytochromes *bd* (*18-22*). However, its precise function and molecular mode of action have remained enigmatic for decades (*3*, *23*). CydDC was initially thought to translocate heme across the bacterial cytoplasmic membrane but later studies raised doubts about this notion and concluded that CydDC is involved in the regulation of the periplasmic redox poise by transporting the reductants glutathione (GSH) and L-cysteine (L-Cys) to the periplasm (*19*, *24-28*). Despite this widely accepted substrate specificity of CydDC, it was later found that the CydDC complex co-purifies with bound heme (*29*). This observation motivated the assumption that heme represents a prosthetic group of a periplasmic redox sensor domain for regulation of transporter activity (*3*, *18*). A recent work fundamentally challenged the transporter function of CydDC and proposed that it operates as a membrane-bound enzyme catalyzing the reduction of cytoplasmic cystine (CSSC) to L-Cys (*30*).

To resolve these points of controversy, we used *Escherichia coli* as a model system amenable to our integrative approach including growth-complementation studies, biochemical activity assays, systematic single-particle electron cryo-microscopy (cryo-EM), and atomistic molecular dynamics (MD) simulations to characterize the function of CydDC down to the atomic level and to dissect its molecular mode of action. For our structural biology approach, we established a matrix of sample conditions based on a combination of putative substrate molecules (GSH, GSSG, L-Cys, CSSC, and heme), nucleotides that are either susceptible or resistant to hydrolysis (ATP, ADP, ADP+Vi, and AMP-PNP), and rationally designed mutant variants of CydDC. We determined 39 individual structures of CydDC under 22 different sample conditions at resolutions of 2.7 to 3.9 Å (Supplementary Table 1,

Supplementary Fig. 1-6). Based on these results, we developed a comprehensive model for the molecular mechanism of CydDC function.

Results

CydDC is required for the biogenesis of both cytochrome *bd* isoforms

We carried out growth complementation studies using the *E. coli* mutant strain MB43, which lacks all terminal oxidases and thus shows impaired respiratory activity (*31*). The growth of this strain is poor compared to wild-type controls, but was improved following the introduction of genes encoding cytochromes *bd*-I (p*cydABX*) or *bd*-II (p*appCBX*) (Fig. 1a, Supplementary Fig. 7). Next, we constructed an isogenic deletion mutant of the *cydDC* operon in the genetic background of MB43. This strain, designated MB43Δ*cydDC*, shows an indistinguishable phenotype to MB43 (Fig. 1a). Unlike MB43 however, the growth of MB43Δ*cydDC* was not restored by introducing p*cydABX* or p*appCBX*. A growth-active phenotype of MB43Δ*cydDC* was only achieved by double complementation with p*cydDC* and either p*cydABX* or p*appCBX.* Accordingly, UV-Vis spectroscopy revealed that the characteristic fingerprints of cytochrome *bd* cofactors (hemes *b* and *d*) were absent in membrane fractions of MB43 and MB43Δ*cydDC* but clearly detected in the growth-restored complementation strains (Fig. 1a-b).
Further, we confirmed oxygen reductase activity of membrane fractions from growth-restored MB43 and MB43Δ*cydDC* variants (Fig. 1c). Finally, we used the highly specific inhibitor aurachin D to confirm that restored oxygen consumption was due to the activity of cytochrome *bd* variants (Fig. 1c). In summary, growth complementation studies, UV-Vis spectroscopy and oxygen consumption assays confirmed that CydDC is essential for the assembly of both known variants of cytochrome *bd* (Fig. 1f).

ATPase activity of CydDC is stimulated by heme

We next tested affinity-purified CydDC for ATPase activity in the presence of various potential substrates, primarily using the Malachite green phosphate assay (Supplementary Fig. 1) (*29*, *30*, *32*, *33*). In agreement with our growth complementation data, but in contrast to previous reports, we found that GSH and L-Cys (and their oxidized counterparts GSSG and CSSC) failed to induce hydrolysis, whereas heme stimulated the ATPase activity of CydDC in a concentration-dependent manner (Fig. 1d-e, Supplementary Fig. 8). This effect is only observed for heme itself, but not for its macrocycle scaffold Protoporphyrin IX, or free iron, suggesting that the complexed iron molecule might play a critical role in binding and coordination. These results were verified by a conceptually different ATP hydrolysis assay based on an enzyme-coupled approach utilizing pyruvate kinase and lactate dehydrogenase (Supplementary Fig. 9). Both assays confirm the ATPase stimulating effect of heme while showing that the tested reductants do not show typical effects of ABC transporter substrates. To bolster our finding of heme as a primary candidate for a substrate molecule of CydDC, we determined kinetic parameters for heme and ATP. We obtained K_M^{app} and V_{max} values of 79.7 nM and 187.04 nmol [Pi] · nmol [CydDC]$^{-1}$ · min^{-1} for heme, and 91.9 μM and 191.58 nmol [Pi] · nmol [CydDC]$^{-1}$ · min^{-1} for ATP (Fig. 1e,

Supplementary Fig. 9). These values are reasonable regarding the physiological occurrence of both substrates.

Next, we generated glutamate to glutamine mutants of the Walker B domains of CydD and CydC to determine whether CydDC possesses a functionally degenerate nucleotide-binding domain (NBD) as found in other ABC transporters (*34*). In case of the CydD^{E511Q}C mutant, we were not able obtain pure and homogeneous preparations of sufficient yield upon recombinant production. In contrast, the CydDC^{E500Q} mutant was stably purified and did not show any reduction in its T_M as compared to the wild-type variant (Supplementary Fig. 1). Using heme as substrate, we showed that the conserved Walker B glutamate of CydC is essential for ATPase activity of CydDC (Fig. 1d, Supplementary Fig. 10-11). In line with this observed lack of enzymatic activity, transformation of MB43Δ*cydDC* with *pE500Q* (CydDC^{E500Q}) in combination with either p*cydABX* or p*appCBX* did not restore bacterial growth (Fig. 1a-b). We thus conclude that NBD^{C} represents the canonical hydrolysis site and that CydD contains a degenerate NBD which presumably fulfils a structural rather than a functional role.

To verify our findings on the role of heme as a potential substrate molecule and to dissect the molecular basis of CydDC function, we employed a systematic single-particle cryo-EM approach for structure determination of CydDC in the presence of different putative substrate molecules, nucleotides, and inhibitors (Supplementary Table 1, Supplementary Fig. 2-6). By solving CydDC structures in biochemically defined states and under turnover conditions, we gained an in-depth view of the conformational landscape and substrate binding modes of this transporter. This allows us to describe key events in substrate recognition, gating, and translocation across the cytoplasmic membrane. In the following, we will focus on the major conformations obtained and their roles in substrate binding, ATP hydrolysis, and substrate release.

General architecture of CydDC

The resting (non-catalytic) inward-facing substrate-free state of CydDC ($\mathbf{IF}^{\mathrm{apo}}_{\mathrm{as\ isolated}}$), which was obtained in conditions lacking any substrate molecule, exhibits canonical features of type IV ABC transporters (Fig. 2) (*35-37*). Each subunit is composed of a membrane domain formed by six transmembrane α-helices (TMH), an N-terminal cytoplasmic elbow helix (EL) oriented parallel to the membrane plane, and a cytoplasmic nucleotide-binding domain (Fig. 2a-b). Both NBDs feature a typical RecA-type fold and two peripheral ABC specific subdomains ABCα and ABCβ (Fig 2a) (*38*). In this conformation the heterodimer adopts an asymmetrical structure with an overall Cα root-mean-square distance (RMSD) of 4.17 Å (TMH: 3.28 Å; NBD: 2.5 Å) (Supplementary Fig. 12). Particularly TMs 4 and

5 show a pronounced conformational difference between CydD and CydC. We address the functional significance between structural symmetry and mechanism of CydDC action later.

Structural insights into substrate specificity

The successful determination of the $\mathbf{IF}^{\text{apo}}_{\text{as isolated}}$ conformation was followed by a systematic screen for substrate molecules that locate within a specific binding pocket. We solved cryo-EM structures of CydDC in the presence of all putative substrate molecules tested in our biochemical assays (GSH, GSSG, L-Cys, CSSC, and heme) (Fig. 2c). Distinct densities within the TMH domain were neither obtained in the presence of reduced nor of oxidized forms of glutathione and L-cysteine. By contrast, we were able to unambiguously identify a bound heme molecule within the TMH domain (Supplementary Fig. 13). This finding is consistent with the ATP hydrolysis inducing effect of heme (Fig. 1d, Supplementary Fig. 9). In addition, we determined structures of CydDC in the presence of a combination of heme and thiols (GSH, GSSG, L-Cys) in order to assess whether these molecules may be heme-dependent co-substrates of CydDC. This possibility was, however, ruled out because we could identify ligand density only for heme but did not observe signal for any other added molecule (Fig. 2c). It is important to note that we obtained heme bound CydDC conformations not only through exogenous heme addition but consistently also from subsets of CydDC particles that natively co-purified with heme in sample compositions free of heme (Fig. 2c). This observation further reinforces our working hypothesis that heme is the physiological substrate of CydDC (Fig. 1f).

Heme binding and occlusion requires sequential conformational transitions

The binding of heme and the formation of an inward-facing confined state requires distinct conformational changes within the TMH domain of CydDC. We obtained three heme-bound states of CydDC that provide comprehensive insight into this process (Fig. 2c, 3, Supplementary Fig. 13-14). Heme first binds to a cavity formed by transmembrane helices $TM2^C$, $TM3^C$, $TM5^D$, and $TM6^D$ that is in the vicinity of the lateral membrane plane (Fig. 3a-b, Supplementary Fig. 13-14). In this $\mathbf{IF}^{\text{heme}}_{\text{bound}}$ conformation, the heme molecule primarily interacts with the invariant $H85^C$ residue which functions as an axial ligand for the heme iron at a distance of 3.4 Å. Additionally, the two heme propionate groups form electrostatic interactions with $R81^C$ of $TM2^C$ and $R136^C$ of $TM3^C$, respectively (Fig. 3b, Supplementary Fig. 13-14). Despite these key interactions, heme is not tightly bound since the distinct density features of the porphyrin macrocycle are less pronounced than the overall local resolution, indicating for a movement dynamic of the substrate (Supplementary Fig. 13). In the subsequent $\mathbf{IF}^{\text{heme}}_{\text{coordinated}}$ conformation, the interaction between CydDC and heme is strengthened by movement of the C-terminal segment of $TM6^D$ toward the heme and concomitant sidechain rearrangements of $H312^D$, which acts as a second axial ligand of the heme iron (Fe - $H312^D$ distance 2.6 Å), and $Y311^D$,

which moves in front of the porphyrin plane and thereby prevents heme from escaping to the membrane space (Fig. 3c, Supplementary Fig. 13-15). The interaction between TM6^{D} and EL^{D} further causes positioning of the elbow helix closer towards TM4^{D}, which narrows the membrane accessible gate to the heme binding site (Supplementary Fig. 13-15). Overall, the TMH region adopts a more compact state upon heme binding and coordination. This compaction is the result of small-scale movements of all transmembrane helices (except TM4^{C} and TM5^{C}) towards the symmetry axis of the TMH domain. The most abundant heme-bound conformation obtained (11 individual structures) is termed $\mathbf{IF}^{\mathrm{heme}}_{\mathrm{confined}}$ and represents the most confined TMH conformation (Fig. 2c, 3d). Upon binding and tight coordination of heme, a crucial conformational change of TM4^{D} is induced. Movement of this 7.2 nm long extended transmembrane helix is occurring on two levels. The membrane embedded segment of TM4^{D} (segment 164-195) changes its angle from ca. 60° to ca. 75° relative to the membrane plane and thus moves in front of the heme, blocking the lateral membrane gate (Supplementary Fig. 15). The kinked C-terminal half of TM4^{D} that is exposed to the cytoplasm concomitantly moves towards EL^{D} and adopts a conformation that runs diagonally above the bound heme molecule (Supplementary Fig. 15). Accordingly, the side chain of F195^{D} moves in front of the heme and aligns in parallel with the porphyrin plane (Fig 3d, Supplementary Fig. 15). Together with Y311 of TM6^{D}, these aromatic residues generate π-π stacking interactions with the porphyrin plane of the heme and thus contribute to the formation of a tightly-sealed substrate access gate (Supplementary Fig. 15). As a consequence, the central solvent-filled cavity of the TMH domain changes in size and position (Fig. 3a-d). The formation of a distinct heme-binding pocket narrows the unoccupied space within the TMH domain and establishes a lateral pathway perpendicular to the membrane plane that ends at the tightly interlocked periplasmic substrate exit gate (Fig. 3d). Furthermore, we observed that if heme was added to CydDC in the absence of nucleotides we exclusively obtained the $\mathbf{IF}^{\mathrm{heme}}_{\mathrm{confined}}$ conformation, which provides evidence that binding and confinement of heme occurs independent of nucleotide occupancy of the NBDs (Fig. 2c).

Based on the deduced sequence of binding events and the distinct interaction patterns between heme and CydDC, we reasoned that the interaction between H85^{C} and the heme iron marks the most crucial step of substrate recognition and initiation of all subsequent events required to facilitate heme translocation across the membrane. To test this hypothesis, we generated a CydDC H85A^{C} mutant (p*H85A*) and performed growth-restoring complementation studies using the MB43Δ*cydDC* strain (Fig. 1a-b). In addition, we investigated the effect of the histidine to alanine replacement on ATP hydrolysis activity of CydDC^{H85A} (Fig. 1d). In both experiments, the results revealed that lack of this highly conserved histidine residue abrogates the functionality of CydDC (Fig. 1a-d, Supplementary Fig. 10). Furthermore, in contrast to wild-type CydDC, CydDC^{H85A} could not be co-purified with bound heme and

could not be loaded with the exogenous addition of heme (Supplementary Fig. 16). These observations were confirmed by the cryo-EM structure of CydDC^{H85A}, which exclusively adopted the $\mathbf{IF}^{\text{apo}}_{\text{as isolated}}$ conformation (Fig. 2c).

Heme accesses CydDC via a membrane pathway and is flipped by 180 degree

To map possible routes of heme entry, we carried out multiple atomistic MD simulations, focusing on the behavior of heme near lipid bilayer surfaces and the substrate binding pocket of CydDC (Fig. 4, Supplementary Fig. 17). As a starting point we placed heme near a heterogeneous membrane composed of 70% POPE, 25% POPG and 5% cardiolipin. In our simulation, heme rapidly partitioned into the lipid bilayer, which is consistent with earlier reports about interactions of heme with biomembranes (Supplementary Fig. 17) (*39*, *40*). The porphyrin scaffold immersed deeply into the membrane core and interacted with lipid acyl chains, while the two propionate groups orientated towards the lipid head groups and interacted mostly with the ethanolamine groups (Supplementary Fig. 17). Next, we analyzed the dynamics of heme placed near the lateral entry site of CydDC in the $\mathbf{IF}^{\text{apo}}_{\text{as isolated}}$ state. Our simulations show that the heme propionates interact with positively charged residues first on the protein surface and then the inside of the binding cavity. These latter interactions induce a rotation of the heme by 90° (Fig. 4). The observation of spontaneous heme binding and rotation suggests this pathway as the primary route for heme entry.

We carried out further MD simulations using models of $\mathbf{IF}^{\text{heme}}_{\text{bound}}$, $\mathbf{IF}^{\text{heme}}_{\text{coordinated}}$, and $\mathbf{IF}^{\text{heme}}_{\text{confined}}$. When heme is placed within the binding pocket without H85^{C}-Fe coordination, it relaxes toward the entry conformation observed after spontaneous heme binding to $\mathbf{IF}^{\text{apo}}_{\text{as isolated}}$ and shows significant mobility within the binding site. However, when heme is axially ligated to H85^{C} in $\mathbf{IF}^{\text{heme}}_{\text{bound}}$, or both H85^{C} and H312^{D} in $\mathbf{IF}^{\text{heme}}_{\text{coordinated}}$ and $\mathbf{IF}^{\text{heme}}_{\text{confined}}$, it maintains the conformation we observed in our cryo-EM structures. We conclude that heme is rotating 90° as it enters the binding site and a further 90° upon binding and axial ligation. This reorientation mechanism may prime heme for directed release toward the periplasmic space or the outer membrane leaflet once the transporter adopts its outward open release conformation (Fig. 4).

These results suggest that CydDC operates via a trap-and-flip mechanism similar to that described for the MFS type proton-dependent lipid transporter LtaA and other primary and secondary active lipid transporters (*41-45*). In MsbA and PfMATE, lipid flipping is primarily driven by electrostatic interactions between lipid head groups and side chains of the respective transporters (*42*, *45*). This functional analogy between lipid and heme flipping indicates that the translocation of amphipathic molecules across biological membranes is presumably based on a common underlying mechanism.

Substrate transport is ATP dependent but not hydrolysis dependent

Next, we aimed to characterize the mechanistic relationship between substate transport and ATP hydrolysis. Active turnover conditions promote two catalytic states as captured by cryo-EM: $\mathbf{IF}_{\mathrm{bound}}^{\mathrm{heme}}$ and a highly asymmetrical heme-free inward-facing conformation with nucleotide bound to both NBDs ($\mathbf{IF}_{\mathrm{asym}}^{\mathrm{apo}}$) (Fig. 2c). Lack of additional conformations suggests that formation of $\mathbf{IF}_{\mathrm{confined}}^{\mathrm{heme}}$ and subsequent translocation of heme to the periplasmic space via outward-facing conformations occurs rapidly and features short-lived intermediate states. To increase chances of capturing transient conformations during the transport cycle, we performed an additional turnover experiment using CydDC^{E500Q} that has a significantly reduced hydrolysis activity (Fig. 1, 2c). This revealed a novel pre-hydrolysis return conformation ($\mathbf{Occ}_{\mathrm{return}}^{\mathrm{apo}}$) following substrate release (Fig. 3h, Supplementary Fig. 14). Surprisingly, the pre-hydrolysis $\mathbf{Occ}_{\mathrm{return}}^{\mathrm{apo}}$ state was only captured by the glutamate to glutamine mutation, but not the use of AMP-PNP instead of ATP, or addition of orthovanadate to wild-type CydDC under active turnover conditions (Fig 2c). In the presence of inhibitors, only the $\mathbf{IF}_{\mathrm{confined}}^{\mathrm{heme}}$ conformation was observed. Notably, the $\mathbf{Occ}_{\mathrm{return}}^{\mathrm{apo}}$ conformation was obtained in all analyzed cryo-EM samples of CydDC^{E500Q} but was enriched in particle population through the addition of heme and ATP. Based on these observations, we conclude that ATP binding but not its hydrolysis is required for the transition from $\mathbf{IF}_{\mathrm{confined}}^{\mathrm{heme}}$ to an outward-facing (**OF**) substate-release state.

Signal transduction and conformational coupling between TMH and NB domains

The transport of heme involves changes in the inter- and intra-subunit symmetry of CydDC. The $\mathbf{IF}_{\mathrm{asym}}^{\mathrm{apo}}$ conformation features the greatest structural asymmetry with an overall Cα RMSD of 5.4 Å (TMH: 3.69 Å; NBD: 1.91 Å) (Supplementary Fig. 12). Loss of symmetry between CydD and CydC in the $\mathbf{IF}_{\mathrm{asym}}^{\mathrm{apo}}$ state is caused by the rotational movement of each subunit along the transporter's central axis perpendicular to the membrane plane. In this wedge-like conformation, the distal side (relative to the heme binding domain) of CydDC moves closer together than the proximal half whereby ABCα^{C} and ABCβ^{D} form a semi-interlocked NBD dimer (Fig. 5a-b). This rearrangement increases the distance between the analogous NBDs of the proximal side, and dilates the heme-accessible membrane cavity (Fig. 3a, 5b). A central question concerning the functionality of ABC transporters is how the information about binding of a substrate molecule to the membrane domain is transduced to the soluble NBDs to induce a fully occluded state for subsequent substrate release and ATP hydrolysis. In CydDC, TM4^{D} has a dual function during the transition from $\mathbf{IF}_{\mathrm{asym}}^{\mathrm{apo}}$ via $\mathbf{IF}_{\mathrm{bound}}^{\mathrm{heme}}$ to $\mathbf{IF}_{\mathrm{confined}}^{\mathrm{heme}}$ state. As described above, the membrane-integrated segment of TM4^{D} strongly contributes to sealing the bound heme molecule from the membrane environment (Fig. 3, Supplementary Fig. 13-15). Beyond this function, we found that movement and rearrangement of the cytoplasmic segment of TM4^{D} is associated with a 25°

rotation of the horizontal coupling helix 2 ($CH2^D$) connecting $TM5^D$ and $TM4^D$. The contact of $CH2^D$ with NBD^C then establishes a conformational coupling that leads to an almost parallel alignment of the two NBDs, which remain separated by ca. 6-8 Å until ATP is bound to the catalytic nucleotide-binding domain of CydC (Fig. 5a).

CydDC features a unique nucleotide exchange mechanism

In $\mathbf{IF}_{\mathrm{asym}}^{\mathrm{apo}}$ we discovered a previously unknown mode of interaction between the CydD signature loop and nucleotide bound to the canonical nucleotide-binding site (NBS) of CydC (Fig. 5). During the asymmetrical interaction of the two NBDs on the distal side, the nucleotide is bound to NBS^C and its adenine base is coordinated by $Y348^C$ of the A-loop via a π - π interaction on one side, and by a π - cation interaction via $R485^D$ of the signature loop from CydD on the opposite side. However, in contrast to previously described fully-interlocked NBD dimers, as for instance from TmrAB (*46*), the signature loop is separated from the γ-phosphate of the nucleotide by 12.6 Å (Fig. 5c, Supplementary Fig. 18). The degenerate NBS^D has a similar geometry in the $\mathbf{IF}_{\mathrm{asym}}^{\mathrm{apo}}$ state, with the exception that adenine does not participate in π - π stacking and π - cation interactions. This is because of the uncharged $L365^D$ residue at the analogous position of $Y348^C$ in the Walker A motif of CydD, and the fact that the signature loop of CydD is placed at a distance of 20 Å to NBS^D (Supplementary Fig. 18). A peculiar and thus far unreported NBS conformation was identified in the $\mathbf{IF}_{\mathrm{confined}}^{\mathrm{heme}}$ state. The conformational coupling between substrate occlusion and signal transduction ($\mathbf{IF}_{\mathrm{asym}}^{\mathrm{apo}}$ to $\mathbf{IF}_{\mathrm{confined}}^{\mathrm{heme}}$) to the NBDs results in the collapse of the NBS^C region and the migration of the Walker A motif into the space originally occupied by the nucleotide phosphate groups (Fig. 5c). During this process, the conformation of NBS^D remains mostly unchanged while the signature loop of CydC moves closer towards the nucleotide, although still separated from it by 10 Å. It is noteworthy that in none of the determined $\mathbf{IF}_{\mathrm{confined}}^{\mathrm{heme}}$ structures, we were able to observe nucleotide bound to NBS^C, even in conditions where nucleotide had been added. In contrast, in all cases where nucleotides were present in the sample, a clear density was identified at NBS^D. This observation suggests that the collapsed conformation of NBS^C lacks affinity for ATP or any other tested nucleotide.

Sequence analysis of critical structural motifs required for ATP hydrolysis did not reveal known mutations that would abolish ATP hydrolysis by NBD^D. However, the tightly interlocked conformation of $\mathbf{Occ}_{\mathrm{return}}^{\mathrm{apo}}$ provides structural insights into differences between NBDs that may explain hydrolysis deficiency of NBD^D (Fig. 5c, Supplementary Fig. 18-19). The primary and presumably most significant difference between ATP bound NBD^D and NBD^C of this pre-hydrolysis state is the respective distance between the switch histidine and the γ-phosphate of ATP. While $H531^C$ is in close distance (2.9 Å) to act as catalytic acid/base during hydrolysis, $H542^D$ is positioned in a less favorable distance of 4.4 Å to participate in polar interactions (Fig. 5c). In addition to this, the weak coordination of the adenosine

base, also found in other heterodimeric ABC transporters, might influence the binding stability of the nucleotide at this position (*46*) (Supplementary Fig. 18-19). With respect to this, it is important to mention that when we determined the $\mathbf{Occ}_{\mathrm{return}}^{\mathrm{apo}}$ state structure from a sample that did not include exogenously added ATP or AMP-PNP, we observed lack of bound nucleotide at NBS^D but not at NBS^C (Fig. 2c, Supplementary Fig. 19). Loss of the NBS^D nucleotide might be possible by the presence of a solvent accessible cavity that remains open towards NBS^D even following the interlocking of NBDs in this conformation, whereas the tight interaction between the A-loop of CydC and ABCα of CydD forms an enclosed inner environment for ATP around NBS^C (Supplementary Fig. 19).

Mechanistic model for substrate release

To complement our cryo-EM data, we modeled important but experimentally inaccessible short-lived conformational states during the transition from $\mathbf{IF}_{\mathrm{confined}}^{\mathrm{heme}}$ to $\mathbf{Occ}_{\mathrm{return}}^{\mathrm{apo}}$. Our simulation-based modelling allowed us to construct three transient CydDC conformations representing distinct states of the transport cycle (Fig. 3e-g). The $\mathbf{Occ}_{\mathrm{confined}}^{\mathrm{heme}}$ state represents heme-loaded CydDC upon ATP binding with tightly interlocked NBDs. To obtain this conformation, we performed an MD simulation for 400 ns of the fully occluded state of CydDC without heme ($\mathbf{Occ}_{\mathrm{return}}^{\mathrm{apo}}$). Further simulations were carried out to generate the $\mathbf{Occ}_{\mathrm{confined}}^{\mathrm{heme}}$ conformation by inserting heme into the binding site using the slow-growth procedure. After generating the initial model, we performed 300 ns of simulation and analyzed the structural stability by RMSD evolution and conformation dynamics. Our final model shows that the transition from $\mathbf{IF}_{\mathrm{confined}}^{\mathrm{heme}}$ to $\mathbf{Occ}_{\mathrm{confined}}^{\mathrm{heme}}$ entails concentered movements of $TM3^C$ and $TM4^D$. This seals the cytoplasmic gate from solvent access and results in a pseudo-symmetric heterodimer conformation (Fig. 3, Extended Data Fig. 14).

Starting from the $\mathbf{Occ}_{\mathrm{confined}}^{\mathrm{heme}}$ and $\mathbf{Occ}_{\mathrm{return}}^{\mathrm{apo}}$ states we obtained two outward-open states ($\mathbf{OF}_{\mathrm{confined}}^{\mathrm{heme}}$ and $\mathbf{OF}^{\mathrm{apo}}$) by performing steered MD simulations on the two periplasmic halves of CydDC. Having generated initial models, we checked the stability and the degree of opening after 300 ns of unrestrained simulations. Our outward facing models suggest that heme is released in a sequential process. First, the periplasmic gate formed by all twelve TMs is opened via separation of two lobes composed of TMs 1-2 of CydC and 4-6 of CydD, and vice versa of TMs 1-2 of CydD and 4-6 of CydC ($\mathbf{OF}_{\mathrm{confined}}^{\mathrm{heme}}$) (Supplementary Fig. 20). These movements cause the lateral cavity next to the heme binding site to enlarge and form an exit pathway. During periplasmic gate-opening we found that the overall interaction of heme with the residues in the binding site remained unchanged. Accordingly, we conclude that substrate release is initiated by retraction of H312 of $TM6^D$ and H85 of $TM2^C$ (Fig. 3, Supplementary Fig. 14). These events most likely change the local affinity and trigger the release towards the periplasmic side of the membrane. The post-release $\mathbf{OF}^{\mathrm{apo}}$ conformation features

a narrower periplasmic gate than $\mathbf{OF}^{\mathrm{heme}}_{\mathrm{confined}}$. With the complete closing of the periplasmic gate, the transporter adopts its pre-hydrolysis $\mathbf{Occ}^{\mathrm{apo}}_{\mathrm{return}}$ conformation as observed in the cryo-EM structures of CydDC^{E500Q} (Fig. 2c, Extended Data Fig. 13). In this state, TM6^{D} and TM2^{C} already adopt the $\mathbf{IF}^{\mathrm{apo}}_{\mathrm{asym}}$ conformation, which would ensure rapid binding of another heme molecule upon ATP hydrolysis and lateral opening of the substrate entry gate (Fig. 3h, Extended Data Fig. 7, Supplementary Movie 13).

Transport cycle

Based on our multi-layered approach, we developed a model for the transport cycle that integrates the results of the employed orthogonal methods (Fig. 6). The cycle starts with the ATP-bound $\mathbf{Occ}^{\mathrm{apo}}_{\mathrm{return}}$ state. We biochemically confirmed that only NBD^{C} is required for the ATPase activity of CydDC (Fig. 1). Hydrolysis of ATP at this site results in mechanochemically-induced return to the substrate-free $\mathbf{IF}^{\mathrm{apo}}_{\mathrm{asym}}$ state (Fig. 3, 5, Supplementary Fig. 14). By this rationale, we assign the densities at NBS^{C} of this post-hydrolysis state obtained from the turnover dataset of CydDC to ADP and Pi (Fig. 5c, Supplementary Fig. 18). We further conclude that heme binding to the TMH domain and ATP to NBD^{C} occurs sequentially rather than simultaneously, given that the binding and occlusion of heme ($\mathbf{IF}^{\mathrm{heme}}_{\mathrm{bound}}$ > $\mathbf{IF}^{\mathrm{heme}}_{\mathrm{coordinated}}$ > $\mathbf{IF}^{\mathrm{heme}}_{\mathrm{confined}}$) is needed to induce dissociation of the distal NBD-NBD interaction, causing NBS^{C} to collapse and release ADP and Pi (Fig. 3-5). Subsequent binding of ATP to NBS^{C} is essential for the transition to the fully occluded $\mathbf{Occ}^{\mathrm{heme}}_{\mathrm{confined}}$ state. This triggers the opening of the extracellular gate, the retraction of TM6^{C}, including the axial heme ligand H312^{D}, to adopt the inward facing conformation of this helix, and the collapsing of the heme binding site ($\mathbf{OF}^{\mathrm{apo}}$) (Fig. 3, 5). After release of the heme to the periplasmic space, the extracellular gate closes again, reverting back to the $\mathbf{Occ}^{\mathrm{apo}}_{\mathrm{return}}$ conformation. The transitional cycle of asymmetrical, symmetry-approaching and pseudo-symmetrical conformations during heme transport is unique to CydDC and highlights the mechanistic possibilities for the specialized substrate transport facilitated by heterodimeric ABC transporters and their diverse conformational space (Supplementary Fig. 21).

Conclusions

The ligand specificity, function and molecular structure of CydDC have been contested for 30 years. The results from various *in vitro* and *in vivo* studies led to conflicting conclusions about its role in bacterial physiology, and its function as a heme transporter was previously ruled out (*21*, *32*, *47*). However, we have now provided comprehensive and direct evidence that the translocation of heme from the cytoplasmic space to the periplasm is the primary role of this ABC transporter. Lack of CydDC is associated with extensive changes in bacterial metabolism, including an over-oxidized periplasm and perturbed respiratory activity (*18*). A crucial link is found between CydDC and the bacterial terminal oxygen reductase cytochrome *bd*, which relies on the function of CydDC for the insertion of its heme

cofactors and functional maturation. This dependency is also reflected in their genomic organization as in most bacteria the structural genes of cytochrome *bd* and CydDC are operonically encoded in the same gene cluster (*48*).

In infection studies, Δ*cydC* mutants of *Mycobacterium tuberculosis and Brucella abortus* displayed diminished survival in mouse models (*49*, *50*). Inactivation of CydDC in *M. tuberculosis* also interfered with bacterial persistence during treatment with the front-line drug isoniazid and caused hypersusceptibility to compounds targeting the mycobacterial bc_1 menaquinol-cytochrome *c* oxidoreductase, with bioenergetic profiles indistinguishable from cytochrome *bd* knock-out strains (*51*, *52*). Hence, CydDC represents a viable target for the development of antibacterial drugs attacking bacterial respiration on the level of assembly.

While our current work provides evidence on a molecular level for the functional link between the heme transport function of CydDC and biogenesis of bacterial cytochromes, two central questions for future research arise. First, are additional and yet unknown periplasmic proteins involved in the process of cytochrome *bd* assembly and cofactor insertion? A putative candidate for a periplasmic chaperone is the heme-binding protein NikA, which is more abundant in *E. coli* strains overexpressing CydDC (*53*). This co-regulation suggests a functional link between CydDC and NikA. However, given the localization of cytochrome *bd* prosthetic heme groups close to the periplasmic membrane surface, it is also conceivable that CydDC could directly interact with the nascent CydA polypeptide and thus might be actively involved in loading heme cofactors to the catalytic subunit of cytochrome *bd*. A first evidence in favor of this scenario is found in *Francisella tularensis*, where a molecular interaction between CydC and CydA was reported based on co-migration patterns in BN-PAGE experiments (*54*). The second question is, whether CydDC functions as a heme scavenger by shifting the equilibrium of membrane-dissolved heme towards the periplasmic leaflet? As shown in previous experimental studies and our MD simulations, partitioning of heme from the aqueous phase into membranes occurs rapidly. However, the transmembrane movement of heme from one bilayer leaflet to the other occurs very slowly ($< 1\ s^{-1}$) (*39*). The kinetic properties of CydDC suggest that heme translocation occurs at much higher rates, indicating that CydDC can shift the equilibrium of membrane-integrated heme towards the periplasmic leaflet. It remains unclear, whether CydDC releases heme to the periplasmic bilayer leaflet, the periplasmic membrane space, or whether it might deliver it directly to another protein. Based on its flippase function, we infer that CydDC could efficiently release heme towards the periplasmic membrane space because the exiting orientation of the heme macrocycle would readily promote electrostatic interactions between the propionate side chains and the periplasmic lipid head groups upon release.

CydDC deletion mutants are also perturbed in the synthesis of cytochrome *b* and *c* (*19*). The ubiquitous cytochrome *c* maturation complex (CcmABCDEFGI) also possesses ATPase activity, and is thought to transport heme actively across the periplasmic membrane (*55*). Given the heme transport function of CydDC and its physiological impact on cytochrome *c* assembly, there may be a functional link between CydDC and the Ccm complex. As of now, it remains unclear whether CcmAB functions as an alternative heme transporter or whether translocation of heme for cytochrome *c* biosynthesis occurs exclusively via CydDC (*56*). Cytochrome *c* defective phenotypes of *E. coli* Δ*cydDC* strains rather support the latter conclusion (*19*, *20*).

Methods

Production of CydDC from *Escherichia coli*

CydDC from *E. coli* was produced in *E. coli* BL21-pLysS (DE3) cells transformed with a pTTQ18 plasmid carrying structural genes of the CydDC heterodimer (*cydD + cydC)* and encoding a C-terminal hexahistidine modification at CydC for downstream IMAC purification (p*cydDC*) (*29*). Mutant variants $CydDC^{E500Q}$ (p*E500Q*), $CydD^{E511Q}C$ (p*E511Q*), and $CydDC^{H85A}$ (p*H85A*) were produced analogously. Further details are found in sequence data provided as supplementary information (Supplementary Table 2-3).

For an initial pre-culture, a volume of 0.1 mL 50% glycerol stock of each respective strain was added to 200 mL M9-Carb (50 µg/mL carbenicillin) growth medium. Cells were incubated at 37 °C while shaking (185 rpm) for 16-20 h. The production culture was started by inoculating 2 L M9-Carb (50 µg/mL carbenicillin) growth medium with the pre-culture adjusted to a starting OD_{600} of 0.1. Cells were grown while shaking (185 rpm) at 37 °C until an OD_{600} of 0.6 before recombinant production was induced by addition of IPTG at a final concentration of 0.6 mM. Gene expression was carried out at 30 °C for 16-18 h. After harvest, cells were disrupted using a French-press cell disruptor (Thermo Fisher Scientific) via double-pass at a pressure of 700-1,000 psi. The cell lysate was centrifuged at 5,000x *g* at 4 °C for 30 minutes. Subsequently, the low-velocity supernatant was centrifuged at 220,000x *g* at 4 °C for 90 minutes. Pelleted membranes were resuspended and stored at a protein concentration of 10 mg/mL in a storage buffer containing 50 mM Tris-HCl (pH 7.4), 100 mM KCl.

Purification of CydDC from *Escherichia coli*

Isolated membranes were solubilized with 1% dodecyl-ß-D-maltoside (DDM) in a mass ratio of 1 mg detergent per 5 mg of membrane protein for 60 minutes at 4 °C. CydDC was purified via His_6-tag affinity chromatography using a Talon (Co-IMAC) affinity matrix (Takara Bio Inc.). For column conditioning and washing step I (10 column volumes [CV]) a buffer containing 50 mM Tris-HCl (pH 8), 500 mM KCl, 10% (v/v) glycerol, 20 mM imidazole, and 0.02% DDM was used. For samples intended to be used for cryo-EM studies, the resin was additionally washed with 10 CV of washing buffer II containing 50 mM Tris-HCl (pH 8), 500 mM KCl, 10% (v/v) glycerol, 20 mM imidazole, and 0.05% LMNG to perform detergent exchange from DDM to LMNG. For step elution (5 x 1 CV), buffers I and II were adjusted to a final imidazole concentration of 300 mM, respectively. For sample polishing, size exclusion chromatography (SEC) was performed using a Superdex 200 10/300 Increase column. The SEC running buffer contained 20 mM MES (pH 6), 50 mM KCl and either 0.02% DDM or 0.001% LMNG. All steps of the purification process were carried out at 4 °C.

Growth complementation studies

The bacterial growth assays were carried out as described previously (*31*). Pre-cultures of *E. coli* MB43 and MB43Δ*cydDC* (transformed with empty pET17 control vector or with plasmids encoding one of the cytochrome *bd* variants and/or CydDC) were incubated in Luria Bertani (LB) medium with 100 µg/mL ampicillin overnight at 37 °C while shaking at 200 rpm. Bacteria were then diluted to OD_{600} of 0.01 with 200 µL LB medium containing 100 µg/mL ampicillin and each sample was subsequently distributed over 8 wells (technical replicates) of a 96-well microtiter plate. OD_{600} was measured every 5 minutes at 37 °C for 20 hours (shaking at 200 rpm) in a SpectraMax Plus 384 Microplate reader (Molecular Devices).

ATP hydrolysis assays

Malachite green phosphate assay

ATPase activity of CydDC was determined colorimetrically as described previously (*57*). In brief, measurements were performed at a final concentration of 50 nM CydDC (in DDM) in a volume of 25 µL and carried out for 5 min at 37 °C. Reactions were stopped by adding 175 µL ice cold stopping buffer (20 mM H_2SO_4) and stored on ice. For detection, 175 µL of a stopped reaction sample was transferred into a 96 well microtiter plate and incubated for 8 min with 50 µL malachite green solution (2.7 mM Malachite Green chloride, 0.17% Tween, 1.5% Na_2MoO_4) at room temperature. The absorbance change at 620 nm was measured by a SpectraMax® M2 Microplate Reader (Molecular Deviced, U.S.A). For heme titration experiments a constant ATP concentration of 1 mM was used. ATP titration experiments were performed at a constant heme concentration of 0.3 µM. Substate screening experiments were performed using following final concentrations of the respective reaction components: ATP (1 mM), ferrous heme (0.5 µM), ferric heme (0.5 µM), protoporphyrin IX (0.5 µM), $FeCl_3$ (0.5 µM), GSH (1 mM), GSSG (1 mM), L-Cys (0.5 mM), CSSC (1 µM), orthovanadate (1 mM), AMP-PNP (1 mM). All measurements were performed in a reaction buffer containing 20 mM Tris-HCl (pH 7.0), 50 mM KCl, 0.02% DDM, and 3 mM $MgCl_2$. Samples without substrate were used as negative control and subtracted as background. All data are presented as mean ± SD (n = 3). Statistical significance was analyzed via paired two-tailed Student's t-tests using the GraphPad t-Test calculator (https://www.graphpad.com/quickcalcs/ttest1/).

Enzyme-coupled ATPase assay

The pyruvate kinase (PK)/lactate dehydrogenase (LDH) coupled ATP hydrolysis assay was performed as described previously (*58*). In brief, a volume of 100 µL activity buffer [20 mM Tris-HCl (pH 7.0), 50 mM KCl, 4 mM $MgCl_2$, 350 µM PEP, 350 µM ATP, 350 µM NADH, 0.02% DDM] was mixed with 2.5 µL PK/LDH enzyme solution (Sigma Aldrich – P0294) and incubated for 5 min at 37 °C in a 96-well microtiter plate. Subsequently, putative substrate candidates and CydDC (0.6 µM final concentration)

were added. Kinetic turnover was monitored at 340 nm for 45 min every 10 s using the SpectraMax® M2 Microplate Reader (Molecular Devices, U.S.A). All data are presented as mean ± SD (n = 3). Statistical significance was analyzed via paired two-tailed Student's t-tests using the GraphPad t-Test calculator (https://www.graphpad.com/quickcalcs/ttest1/).

Determination of thermal stability by microscale thermophoresis

Thermal stabilities of purified CydDC variants were investigated with a Prometheus NT.48 instrument (Nanotemper). Excitation at 280 nm (20 nm bandwidth) was set to a power of 10% yielding emission intensities of 6,000 to 25,000 at 333-380 nm. A temperature ramp of 1 °C/min between 20 and 95 °C was applied in all experiments. Measurements were performed at 2 µM CydDC concentration. Heme was added in equimolar concentrations to CydDC. Unfolding transitions were monitored from changes in the emission of tryptophan and tyrosine fluorescence at 350/330 nm. Melting temperatures were determined at the inflection points (free energy change ΔG is equal to zero) from the raw data (measured in triplicates) after baseline correction and normalization.

Cryo-EM sample preparation

In order to collect cryo-EM data of CydDC in different sample conditions, different combinations of CydDC variants, nucleotides, inhibitors, and putative substrate molecules were prepared. See Supplementary Fig. 5 for details of specific sample conditions. For all non-turnover datasets, the protein concentration was adjusted to approximately 1.5 mg/mL before other components were added. Heme loading was performed prior to sample vitrification. Heme was adjusted to a final concentration of 17 µM in all heme containing samples. Nucleotides and inhibitors (ADP, AMP-PNP, and orthovanadate) were used at a final concentration of 1 mM (+ 2 mM $MgCl_2$). Putative substrate molecules were screened at final concentrations of 1 mM. Due to poor aqueous solubility cystine was adjusted to the highest possible final concentration of 0.2 mM. Samples were incubated for 2 minutes at room temperature before plunge freezing.

For preparation of turnover samples, the protein concentration was adjusted to 3 mg/mL. Subsequently, heme was added at a final concentration of 34 µM. The sample was then mixed with a freshly prepared ATPase buffer [20 mM MES (pH 6), 50 mM KCl, 0.001% LMNG, 10 mM ATP and 20 mM $MgCl_2$) in a ratio of 1:1, incubated for 30 seconds at 37 °C, and immediately subjected to plunge freezing. Identical plunge freezing conditions were applied for all samples: Quantifoil R1.2/1.3 copper grids (mesh 300) were washed in chloroform and subsequently glow discharged twice with a PELCO easiGlow device at 15 mA for 45 seconds. A volume of 4 µL sample was applied to a grid and blotting was performed for 4 seconds at 4 °C, 100% humidity with nominal blot force 20 immediately before freezing in liquid ethane, using a Vitrobot Mark IV device (Thermo Scientific).

Cryo-EM image recording

For each cryo-EM sample, a dataset was recorded in Energy-Filtered Transmission Electron Microscopy (EF-TEM) mode using either a Titan Krios G2 or a Krios G3i microscope (Thermo Scientific), both operated at 300 kV. Electron-optical alignments were adjusted with EPU 2.9 - 2.11 (Thermo Scientific). Images were recorded using automation strategies of EPU 2.9 - 2.11 in electron counting mode with either a Gatan K2 (installed on Krios G2) or a Gatan K3 (installed on Krios G3i) direct electron detector at a nominal magnification of 105,000, corresponding to a calibrated pixel size of 0.831 Å and 0.837 Å, respectively. Dose fractionated movies (40 frames) were recorded at an electron flux of approximately 15 e^- x $pixel^{-1}$ x s^{-1} for 2 s, corresponding to a total dose of ~40 e^-/A^2. Images were recorded between -1.1 and -2.1 µm nominal defocus.

Cryo-EM image processing

For each acquired dataset, the same cryo-EM image processing approach was applied: MotionCor2 was used to correct for beam-induced motion and to generate dose-weighted images (*59*). Gctf was used to determine the contrast transfer function (CTF) parameters and perform correction steps (*60*). Images with estimated poor resolution (>4 Å) and severe astigmatism (>400 Å) were removed at this step. Particles were picked by crYOLO and used for all further processing steps (*61*). 2D classification and initial model building were performed using RELION-3.1 (*62*). The initial model obtained from dataset 1 was used for all subsequent datasets. 3D classification, CTF refinement, Bayesian polishing, 3D classification without alignment, and final map reconstructions were performed with RELION-3.1. All Fourier shell correlation (FSC) curves were generated in RELION-3.1. Local-resolution estimation was performed in RELION-3.1 for all final maps. A detailed overview of our processing workflow, and a summary of map qualities are shown in Supplementary Fig. 4-6.

Model building and geometry refinement

The first atomic model of CydDC was built *de novo* into the EM density map in Coot (version 0.8) (*63*). After manual backbone tracing and docking of side chains in the respective map densities real-space refinement in Phenix was performed (version 1.18) (*64*). Refinement results were manually inspected and corrected if required. This model was used as a template to build all subsequent atomic models. In total, 21 models were built, refined, inspected and corrected. The finalized models were validated by MolProbity implemented in Phenix (*65*). Map-to-model cross validation was performed in Phenix (version 1.18). $FSC_{0.5}$ was used as cut-off to define resolution. A summary of model parameters and the corresponding cryo-EM map statistics is found in Supplementary Table 1. The finalized models

were visualized using ChimeraX (*66*). Highest resolution models of $\mathbf{IF}^{\mathrm{apo}}_{\mathrm{asym}}$, $\mathbf{IF}^{\mathrm{heme}}_{\mathrm{bound}}$, $\mathbf{IF}^{\mathrm{heme}}_{\mathrm{coordinated}}$, $\mathbf{IF}^{\mathrm{heme}}_{\mathrm{confined}}$, and $\mathbf{Occ}^{\mathrm{apo}}_{\mathrm{return}}$ were used for MD simulations.

Tunnels and interior cavities

Tunnels and cavities were mapped with MOLE 2.5 (bottleneck radius: 1.2 Å, bottleneck tolerance 3 Å, origin radius 5 Å, surface radius 10 Å, probe radius 5 Å, interior threshold 1.1 Å) (*67*).

Structural alignments

The overall folds of the CydDC subunits CydC and CydD were compared with each other using the structural alignment program TM-align (*68*). Subunits, individual transmembrane regions, and NBDs were aligned and respective Cα R.M.S.D values were calculated.

Molecular dynamics simulations

The CydDC structures were placed in a heterogenous bilayer composed of POPE (70%),POPG (25%), and CL (5%) using CHARMM-GUI (*69*). All systems were hydrated with 150 mM NaCl electrolyte. The all-atom CHARMM36m force field was used for lipids, ions, cofactors, and protein with TIP3P water (*70*, *71*). MD trajectories were analyzed using Visual Molecular Dynamics (VMD) (*72*) and MDAnalysis (*73*).

All simulations were performed using GROMACS 2021.2 (*74*). Starting systems were energy-minimized for 5,000 steepest descent steps and equilibrated initially for 500 ps of MD in a canonical (NVT) ensemble and later for 7.5 ns in an isothermal-isobaric (NPT) ensemble under periodic boundary conditions. During equilibration, the restraints on the positions of nonhydrogen protein atoms of initially 4,000 $kJ{\cdot}mol^{-1}{\cdot}nm^{2}$ were gradually released. Particle-mesh Ewald summation (*75*) with cubic interpolation and a 0.12-nm grid spacing was used to treat long-range electrostatic interactions. The time step was initially 1 fs, and was increased to 2 fs during the NPT equilibration. The LINCS algorithm was used to fix all bond lengths (*76*). Constant temperature was established with a Berendsen thermostat, combined with a coupling constant of 1.0 ps. A semi-isotropic Berendsen barostat was used to maintain a pressure of 1 bar (*77*). During production runs, the Berendsen thermostat and barostat were replaced by a Nosé–Hoover thermostat and a Parrinello–Rahman barostat (*78*, *79*). Analysis was carried out on unconstrained simulations. Simulations with liganded and unliganded heme were performed for 400 ns for each of $\mathbf{IF}^{\mathrm{heme}}_{\mathrm{bound}}$, $\mathbf{IF}^{\mathrm{heme}}_{\mathrm{coordinated}}$, and $\mathbf{IF}^{\mathrm{heme}}_{\mathrm{confined}}$ states.

For heme entry simulations a heterogenous bilayer composed of POPE (70%),POPG (25%), and CL (5%) was built using CHARMM-GUI (*69*). The system was hydrated with 150 mM NaCl electrolyte. After 7 ns of equilibration, a production run was performed for 100 ns. Then, a heme molecule (ferrous state)

was placed 1 nm away from the membrane. Ten separate MD simulations were initiated with independent initial velocities drawn according to the Boltzmann distribution of the targeted temperature. Each replicate was run for additional 100 ns. In seven out of the ten simulations, the heme molecule had partitioned into the membrane bilayer at the end of 100ns simulation. The $\mathbf{IF}^{\text{apo}}_{\text{as isolated}}$ CydDC structure was placed in a heterogenous bilayer composed of POPE (70%), POPG (25%), and CL (5%) using CHARMM-GUI (*69*). Then, a heme molecule was placed near the lateral opening between $TM4^D$ and $TM6^D$ in 5 different positions. After equilibration, a simulation of 100 ns duration was performed for each setup.

We modeled the $\mathbf{Occ}^{\text{heme}}_{\text{confined}}$ state, which represents the heme-loaded conformation of CydDC upon ATP binding, with tightly interlocked NBDs. To obtain this conformation, we first ran an MD simulation for the fully occluded state of CydDC without heme ($\mathbf{Occ}^{\text{apo}}_{\text{return}}$) for 400 ns to get an equilibrated structure in the membrane bilayer. Then, the end structure of this simulation was aligned with the $\mathbf{IF}^{\text{heme}}_{\text{confined}}$ conformation and a virtual heme molecule was placed in the approximate position of the binding site taken from the aligned $\mathbf{IF}^{\text{heme}}_{\text{confined}}$ conformation. In the next step, three independent simulations were carried out to generate the $\mathbf{Occ}^{\text{heme}}_{\text{confined}}$ conformation by gradually turning on the interactions of the virtual heme with the protein and the rest of the system. Increasing a lambda parameter scaling these interactions slowly from 0 to 1, over 1 ns with a 0.5 fs timestep, results in the insertion of heme by slow growth. This method allows for smooth adaptation of amino acids in the binding site to the presence of heme. Extra position restraints were added to the C-alpha atoms of the NBDs to stabilize the conformation of protein during the slow-growth process. After the slow-growth heme insertion, we added the axial ligation bonds between heme and $H85^C$ and $H312^D$ and energy minimized the system. Then, we performed 300 ns of simulation. Structural stability during simulations was checked by RMSD evolution and conformation dynamics.

To obtain the two elusive outward-open ($\mathbf{OF}^{\text{heme}}_{\text{confined}}$ and $\mathbf{OF}^{\text{apo}}$) states, we performed steered MD simulations starting from $\mathbf{Occ}^{\text{heme}}_{\text{confined}}$ and $\mathbf{Occ}^{\text{apo}}_{\text{return}}$, respectively. A bias was applied on the distance between the center of mass of the two periplasmic halves of CydDC. The periplasmic halves are defined as (i) TM 1-2 of CydC and TM 3-6 of CydD and (ii) TM 1-2 of CydD and TM 3-6 of CydC. The initial value of the distance was 19 Å and the target value was 28 Å (based on the outward-open structure of TmrAB PBD ID 6RAJ). The steered MD was performed in PLUMED-patched Gromacs with an approximate velocity of 0.01 nm/ns. The steered MD simulation was performed for 100 ns. After the simulation and full opening of the periplasmic side, we ran a further 50 ns of restrained simulation which allowed the lipid molecules around the periplasmic site to equilibrate around the new conformation. Later, we

performed a further 200 ns of unrestrained simulation for each of the two conformations. Finally, we checked the stability and the degree of opening after 300 ns of unrestrained simulations.

Preparation of membrane fractions for heme spectra and oxygen consumption assays

Membrane fractions were isolated as described previously (*80*). In brief, *E. coli* strains were grown in 800 mL LB medium (2-liter baffled flasks) from a starting OD_{600} of 0.01 until late exponential phase. After washing with phosphate buffer saline, batches of cells (5 g) were resuspended in a buffer composed of 50 mM MOPS (pH 7), 100 mM NaCl, and cOmplete protease inhibitor (Roche) in a ratio of 5:1. Cells were disrupted using a Stansted homogenizer at 1.2 kbar. Cell debris was removed centrifugation at 9,500× *g* for 20 min at 4 °C. Membrane fractions were collected by ultracentrifugation at 250,000× *g* for 75 min at 4 °C. Membranes were resuspended in the above buffer containing 0.025% n-dodecyl-β-D-maltoside (DDM), and used for downstream oxygen consumption activity assays and spectroscopic analysis of heme cofactors.

Ultraviolet-visible (UV-Vis) absorption spectroscopy for heme identification

The heme composition of membrane fractions was analyzed by reduced minus oxidized UV-Vis spectra based on Goojani *et al.* (*31*). Membrane fractions were diluted to a protein concentration of 2.6 mg/mL in a buffer composed of 10 mM Tris (pH 7.4) and 16 mM sodium cholate. Samples were first oxidized with 100 µM potassium ferricyanide and a spectrum was recorded at room temperature using a Varian Cary 50 UV-Vis Spectrophotometer. Subsequently, a few grains of solid sodium hydrosulfite were dissolved in the sample to measure the spectrum in the fully reduced state. The difference spectrum (reduced-oxidized) was calculated using Origin Lab Pro 9.5 (Additive GmbH, Germany).

Oxygen consumption measurements

The oxygen consumption activity of membrane fractions was measured using a Clark-type electrode based on Goojani *et al* (*31*). The membrane fractions were adjusted to a concentration of 0.01 - 0.03 mg/mL using a buffer composed of 50 mM MOPS (pH 7.0), 100 mM NaCl, and 0.025% DDM. Subsequently, the membrane fractions were pre-incubated with either aurachin D (final concentration 400 nM) or with DMSO as control for 3 min in the electrode chamber. Ubiquinone-1 and dithiothreitol (DTT) were pre-incubated separately for 3 min and then injected into the electrode chamber to start the reaction (final conc.: 200 µM ubiquinone-1 and 10 mM DTT). The reaction rate was determined for the period between 90 s and 150 s after addition of the substrate mixture. Statistical significance was analyzed via paired two-tailed Student's t-tests using the GraphPad t-test calculator (https://www.graphpad.com/quickcalcs/ttest1/).

Multiple sequence alignments

Multiple sequence alignments of CydD and CydC from *Escherichia coli* (strain K12), *Mycobacterium tuberculosis* (strain ATCC 25618 / H37Rv), *Mycobacterium smegmatis* MC2-155, *Mycobacterium bovis* (strain ATCC BAA-935/AF2122/97), *Corynebacterium glutamicum*, *Brucella abortus biovar*, *Shewanella violacea* (strain JCM 10179/CIP 106290/LMG 19151/DSS12), *Geobacillus stearothermophilus*, and *Klebsiella pneumoniae* were performed using Clustal Omega (*81*) and visualized using Jalview v. 2.11.2.0.

Data availability

Cryo-EM maps are deposited at the Electron Microscopy Data Bank under accession numbers: EMD-14636, EMD-14638, EMD-14639, EMD-14640, EMD-14641, EMD-14642, EMD-14643, EMD-14644, EMD-14645, EMD-14646, EMD-14647, EMD-14649, EMD-14652, EMD-14653, EMD-14654, EMD-14655, EMD-14656, EMD-14657, EMD-14659, EMD-14660, EMD-14661, EMD-14662, EMD-14663, EMD-14665, EMD-14667, EMD-14668, EMD-14669, EMD-14670, EMD-14671, EMD-14672, EMD-14673, EMD-14674, EMD-14675, EMD-14676, EMD-14677, EMD-14681, EMD-14683, EMD-14684, EMD-14689. Atomic models of CydDC have been deposited to the Protein Data Bank under accession numbers: 7ZD5, 7ZDA, 7ZDB, 7ZDC, 7ZDE, 7ZDF, 7ZDG, 7ZDK, 7ZDL, 7ZDO, 7ZDR, 7ZDS, 7ZDT, 7ZDU, 7ZDV, 7ZDW, 7ZDX, 7ZE2, 7ZE4, 7ZE5, 7ZEC.

All other data is presented in the main text or supplementary materials. Source data are provided with this paper.

Acknowledgements

We thank Alexander Hahn and Gregory Cook for valuable discussions. We thank Hartmut Michel for support and providing infrastructural resources. **Funding:** This work was supported by the Max Planck Society, the Nobel Laureate Fellowship of the Max Planck Society, and the Deutsche Forschungsgemeinschaft (Cluster of Excellence Macromolecular Complexes Frankfurt).

Author contributions

D.W purified CydDC, prepared grids, collected cryo-EM data, processed cryo-EM data, refined the structure, built the model, co-drafted the manuscript, and prepared figures. F.F purified CydDC, prepared grids, collected cryo-EM data, performed biochemical activity assays, analyzed data, and drafted figures. H.G.G performed bacterial growth assays, determined oxygen consumption rates, and collected UV-Vis spectra. A.R.M performed MD simulations, co-drafted the manuscript, and prepared figures. T.N.G performed biochemical activity assays and analyzed data. R.G optimized purification conditions and performed initial cryo-EM screening experiments. T.R implemented purification and optimized CydDC buffer conditions. R.Z assisted in cell culturing and protein purification. M.S provided p*cydDC* and p*H85A*, and established the enzyme coupled ATPase assay. S.W calibrated and aligned the microscope. M.S and S.S initiated the project. G.H, D.B, M.S, and S.S supervised the project. S.S designed research, evaluated data, funded the project, drafted the manuscript, and generated figures.

Competing interests

The authors declare no conflict-of-interest.

References

1. Zhang Li, Heme biology: the secret life of heme in regulating diverse biological processes, *Singapore: World Scientific* (2011).
2. Zhang Li, Heme biology: heme acts as a versatile signaling molecule regulating diverse biological processes, *Singapore: World Scientific* (2020).
3. Mark Shepherd. The CydDC ABC transporter of *Escherichia coli*: new roles for a reductant efflux pump. *Biochemical Society Transactions* **43,** 908–912 (2015).
4. Lindley, P- F. Iron in biology: A structural viewpoint. *Reports on Progress in Physics* **59,** 867–933 (1996).
5. Ganz, T. & Nemeth, E. Iron homeostasis in host defense and inflammation. *Nature Reviews Immunology* **15,** 500–510 (2015).
6. Andrews, N. C. Iron metabolism: Iron deficiency and iron overload. *Annual Review of Genomics and Human Genetics* **1,** 75–98 (2000).
7. Andrews, S. C. *et al*. Bacterial iron homeostasis. *Fems Microbiology Reviews* **27,** 215–237 (2003).
8. Lienemann, M. Molecular mechanisms of electron transfer employed by native proteins and biological-inorganic hybrid systems. *Computational and Structural Biotechnology Journal* **19,** 206–213 (2020).
9. Safarian, S. *et al.* Active site rearrangement and structural divergence in prokaryotic respiratory oxidases. *Science* **366,** 100–104 (2019).
10. Safarian, S. *et al.* The cryo-EM structure of the *bd* oxidase from *M. tuberculosis* reveals a unique structural framework and enables rational drug design to combat TB. *Nat. Commun.* **12,** 5236 (2021).
11. Kolbe, F.*et al*. Cryo-EM structures of intermediates suggest an alternative catalytic reaction cycle for cytochrome c oxidase *Nat. Commun.* **12,** 6903 (2021).
12. Buschmann, S. *et al.* The structure of cbb3 cytochrome oxidase provides insights into proton pumping. *Science* **329,** 327–330 (2010).
13. Abramson, J. *et al.* The structure of the ubiquinol oxidase from *Escherichia coli* and its ubiquinone binding site. *Nat. Struct. Biol.* **7,** 910–917 (2000).
14. Soulimane, T. *et al.* Structure and mechanism of the aberrant *ba*3-cytochrome *c* oxidase from *Thermus thermophilus*. *The EMBO Journal* **19,** 1766–1776 (2000).
15. Grund, T. N. *et al.* Mechanistic and structural diversity between cytochrome *bd* isoforms of *Escherichia coli*. *PNAS* **118,** e2114013118 (2021).
16. Mascolo, L. & Bald, D. Cytochrome *bd* in *Mycobacterium tuberculosis*: A respiratory chain protein involved in the defense against antibacterials. *Progress in Biophysics and Molecular Biology* **152,** 55–63 (2020).
17. Bald, D. *et al.* Targeting energy metabolism in *Mycobacterium tuberculosis*, a new paradigm in antimycobacterial drug discovery. *mBio* **8,** 159 (2017).
18. Holyoake, L. V. *et al.* The CydDC family of transporters and their roles in oxidase assembly and homeostasis. *Advances in Microbial Physiology* **66,** 1–53 (2015).
19. Poole, R. K. *et al*. The Cydd gene product, component of a heterodimeric ABC Transporter, is required for assembly of periplasmic cytochrome c and of cytochrome *bd* in *Escherichia coli*. *FEMS Microbiology Letters* **117,** 217–224 (1994).
20. Goldman, B. S. *et al*. Use of heme reporters for studies of cytochrome biosynthesis and heme transport. *Journal of Bacteriology* **178,** 6338–6347 (1996).
21. Georgiou, C. D. *et al*. Identification of the cydC locus required for expression of the functional form of the cytochrome *d* terminal oxidase complex in *Escherichia coli*. *Journal of Bacteriology* **169**, 2107-2112 (1987).
22. Bebbington, K. J. & Williams, H. D. Investigation of the role of the *cydD* gene product in production of a functional cytochrome *d* oxidase in *Escherichia coli*. *FEMS Microbiology Letters* **112,** 19–24 (1993).
23. Poole, R. K. *et al.* Cytochrome *bd* biosynthesis in *Escherichia coli*: the sequences of the *cydC* and *cydD* genes suggest that they encode the components of an ABC membrane transporter. *Molecular Microbiology* **10,** 421–430 (1993).
24. Georgiou, C. D. *et al*. Identification of the *cydC* locus required for expression of the functional form of the cytochrome *d* terminal oxidase complex in *Escherichia coli*. *Journal of Bacteriology* **169,** 2107–2112 (1987).
25. Pittman, M. S. *et al*. A bacterial glutathione transporter (*Escherichia coli* CydDC) exports reductant to the periplasm. *J. Biol. Chem.* **280,** 32254–32261 (2005).
26. Pittman, M. S. *et al.* Cysteine is exported from the *Escherichia coli* cytoplasm by CydDC, an ATP-binding cassette-type transporter required for cytochrome assembly. *J. Biol. Chem.* **277,** 49841–49849 (2002).

27. Goldman, B. S. *et al*. The temperature-sensitive growth and survival phenotypes of *Escherichia coli cydDC* and *cydAB* strains are due to deficiencies in cytochrome *bd* and are corrected by exogenous catalase and reducing agents. *Journal of Bacteriology* **178**, 6348-6351 (1996).
28. Holyoake, L. V. *et al.* CydDC-mediated reductant export in *Escherichia coli* controls the transcriptional wiring of energy metabolism and combats nitrosative stress. *Biochem. J.* **473,** 693–701 (2016).
29. Yamashita, M. *et al.* Structure and function of the bacterial heterodimeric ABC transporter CydDC: stimulation of ATPase activity by thiol and heme compounds. *J. Biol. Chem.* **289,** 23177–23188 (2014).
30. Mironov, A. *et al.* CydDC functions as a cytoplasmic cystine reductase to sensitize *Escherichia coli* to oxidative stress and aminoglycosides. *PNAS* **117,** 23565–23570 (2020).
31. Goojani, H. G. *et al.* The carboxy-terminal insert in the Q-loop is needed for functionality of *Escherichia coli* cytochrome *bd*-I. *Biochimica et Biophysica Acta (BBA) - Bioenergetics* **1861,** 148175 (2020).
32. Pittman, M. S. *et al.* Cysteine is exported from the *Escherichia coli* cytoplasm by CydDC, an ATP-binding cassette-type transporter required for cytochrome assembly. *J. Biol. Chem.* **277,** 49841–49849 (2002).
33. Cruz-Ramos H. *et al.* Membrane topology and mutational analysis of *Escherichia coli* CydDC, an ABC-type cysteine exporter required for cytochrome assembly. *Microbiology* **150,** 3415–3427 (2004).
34. Stockner, T. *et al*. The role of the degenerate nucleotide binding site in type I ABC exporters. *FEBS Lett.***594**, 3815-3838 (2020).
35. Thomas, C. *et al*. Structural and functional diversity calls for a new classification of ABC transporters. *FEBS Lett.***594**, 3767-3775 (2020).
36. Hohl, M. *et al*. Crystal structure of a heterodimeric ABC transporter in its inward-facing conformation. *Nat Struct Mol Biol.* **25**, 395-402 (2012).
37. Noell, A. *et al.* Crystal structure and mechanistic basis of a functional homolog of the antigen transporter TAP. *PNAS* **114,** E438–E447 (2017).
38. Oswald, C. *et al*. The motor domains of ABC-transporters. What can structures tell us? *Naunyn Schmiedebergs Arch Pharmacol.* **372**, 389-399 (2006).
39. Light WR 3rd. *et al.* Transmembrane movement of heme. *J. Biol. Chem.* **265,** 15623–15631 (1990).
40. Light WR 3rd. *et al.* The effects of lipid composition on the rate and extent of heme binding to membranes. *J. Biol. Chem.* **265,** 15632–15637 (1990).
41. Olsen, J. A. *et al.* Structure of the human lipid exporter ABCB4 in a lipid environment. *Nat Struct Mol Biol.* **27,** 62–70 (2020).
42. Mi, W. *et al.* Structural basis of MsbA-mediated lipopolysaccharide transport. *Nature* **549,** 233–237 (2017).
43. Kim, Y. & Chen, J. Molecular structure of human P-glycoprotein in the ATP-bound, outward-facing conformation. *Science* **359**, 915-919 (2018).
44. Lambert, E. *et al.* Evidence for a trap-and-flip mechanism in a proton-dependent lipid transporter. *Nature Communications* **13,** 1–13 (2022).
45. Zakrzewska S. *et al.* Inward-facing conformation of a multidrug resistance MATE family transporter. *PNAS* **116**, 12275-12284 (2019).
46. Hofmann, S. *et al.* Conformation space of a heterodimeric ABC exporter under turnover conditions. *Nature* **571,** 580–583 (2019).
47. Goldman, B. S. *et al.* The temperature-sensitive growth and survival phenotypes of *Escherichia coli cydDC* and *cydAB* strains are due to deficiencies in cytochrome *bd* and are corrected by exogenous catalase and reducing agents. *Journal of Bacteriology* **178**, 6348-6351 (1996).
48. Esposti, M. D. *et al.* Molecular evolution of cytochrome *bd* oxidases across proteobacterial genomes. *Genome Biol Evol.* **7,** 801–820 (2015).
49. Shi, L. *et al.* Changes in energy metabolism of *Mycobacterium tuberculosis* in mouse lung and under in vitro conditions affecting aerobic respiration. *PNAS* **102,** 15629–15634 (2005).
50. *Brucella abortus* Δ*cydC*Δ*cydD* and Δ*cydC*Δ*purD* double-mutants are highly attenuated and confer long-term protective immunity against virulent *Brucella abortus*. *Vaccine* **34,** 237–244 (2016).
51. Moosa, A. *et al.* Susceptibility of *Mycobacterium tuberculosis* cytochrome *bd* oxidase mutants to compounds targeting the terminal respiratory oxidase, cytochrome *c*. *Antimicrobial Agents and Chemotherapy* **61,** e01338-17 (2017).
52. Dhar N. & McKinney JD. *Mycobacterium tuberculosis* persistence mutants identified by screening in isoniazid-treated mice. *PNAS* **107**, 12275-12280 (2010).
53. Shepherd, M. *et al.* NikA binds heme: A new role for an *Escherichia coli* periplasmic nickel-binding protein. *Biochemistry* **46,** 5030–5037 (2007).
54. Dresler J. *et al. Francisella tularensis* membrane complexome by blue native/SDS-PAGE. *Journal of Proteomics* **75,** 257–269 (2011).

55. Sanders, *et al.* Cytochrome *c* biogenesis: the Ccm system. *Trends in Microbiology* **18,** 266–274 (2010).
56. Schulz, H. *et al.* Heme transfer to the heme chaperone CcmE during cytochrome *c* maturation requires the CcmC protein, which may function independently of the ABC-transporter CcmAB. *PNAS* **96,** 6462–6467 (1999).
57. Morbach, S. *et al.* The ATP-binding cassette (ABC) transporter for maltose/maltodextrins of Salmonella typhimurium. Characterization of the ATPase activity associated with the purified MalK subunit. *J. Biol. Chem.* **268**, 18617–18621 (1993).
58. Yun CH. *et al.* The T790M mutation in EGFR kinase causes drug resistance by increasing the affinity for ATP. *PNAS* **105**, 2070-2075 (2008).
59. Zheng, S. Q. *et al*. MotionCor2: anisotropic correction of beam-induced motion for improved cryo-electron microscopy. *Nat Methods.* **14**, 331-332 (2017).
60. Zhang K. Gctf: Real-time CTF determination and correction. *Journal of Structural Biology* **193,** 1–12 (2016).
61. Wagner, T. *et al.* SPHIRE-crYOLO: A fast and well-centering automated particle picker for cryo-EM. *Commun Biol.* **2**, 218 (2018).
62. Scheres, S. H. W. RELION: Implementation of a Bayesian approach to cryo-EM structure determination. *Journal of Structural Biology* **180,** 519–530 (2012).
63. Emsley, P. *et al*. IUCr. Features and development of Coot. *Acta Crystallogr Sect D Biol Crystallogr* **66,** 486–501 (2010).
64. Adams, P. D. *et al.* PHENIX: a comprehensive Python-based system for macromolecular structure solution. *Acta Crystallogr Sect D Biol Crystallogr* **66,** 213–221 (2010).
65. Chen, V. B. *et al.* MolProbity: all-atom structure validation for macromolecular crystallography. *Acta Crystallogr Sect D Biol Crystallogr* **66,** 12–21 (2010).
66. Goddard, T. D. *et al.* UCSF ChimeraX: Meeting modern challenges in visualization and analysis. *Protein Science* **27,** 14–25 (2018).
67. Sehnal, D. *et al.* MOLE 2.0: advanced approach for analysis of biomacromolecular channels. *Journal of cheminformatics* **5,** 39–39 (2013).
68. Zhang Y & Skolnick J. TM-align: a protein structure alignment algorithm based on the TM-score. *Nucleic Acids Res.* **33***,* 2302-2309 (2005).
69. Wu, E. L. *et al.* CHARMM-GUI Membrane Builder toward realistic biological membrane simulations. *Journal of Computational Chemistry* **35,** 1997–2004 (2014).
70. Olsson, M. H. M. *et al.* PROPKA3: Consistent Treatment of Internal and Surface Residues in Empirical pKa Predictions. *J Chem Theory Comput.* **7**, 525-537 (2011).
71. Jorgensen, W. L. *et al.* Comparison of simple potential functions for simulating liquid water. *The Journal of Chemical Physics* **79,** 926 (1998).
72. Humphrey W. *et al.* VMD: Visual molecular dynamics. *Journal of Molecular Graphics* **14,** 33–38 (1996).
73. Agrawal, N. M. *et al.* MDAnalysis: A toolkit for the analysis of molecular dynamics simulations. *Journal of Computational Chemistry* **32,** 2319–2327 (2011).
74. Abraham M. J. *et al.* GROMACS: High performance molecular simulations through multi-level parallelism from laptops to supercomputers. *SoftwareX* **1-2,** 19–25 (2015).
75. Darden, T. *et al.* Particle mesh Ewald: An N·log(N) method for Ewald sums in large systems. *The Journal of Chemical Physics* **98,** 10089 (1998).
76. Hess, B. *et al.* LINCS: A linear constraint solver for molecular simulations. *Journal of Computational Chemistry* **18,** 1463–1472 (1997).
77. Berendsen, H. J. C. *et al.* Molecular dynamics with coupling to an external bath. *The Journal of Chemical Physics* **81,** 3684 (1998).
78. Hoover, W. G. Canonical dynamics: Equilibrium phase-space distributions. *Phys. Rev. A* **31,** 1695 (1985).
79. Parrinello, M. & Rahman, A. Polymorphic transitions in single crystals: A new molecular dynamics method. *Journal of Applied Physics* **52,** 7182 (1998).
80. Hoeser, J. *et al.* Subunit CydX of *Escherichia coli* cytochrome *bd* ubiquinol oxidase is essential for assembly and stability of the di-heme active site. *FEBS Letters* **588,** 1537–1541 (2014).
81. Sievers, F. *et al.* Fast, scalable generation of high-quality protein multiple sequence alignments using Clustal Omega. *Molecular Systems Biology* **7,** 539–539 (2011).

Figures

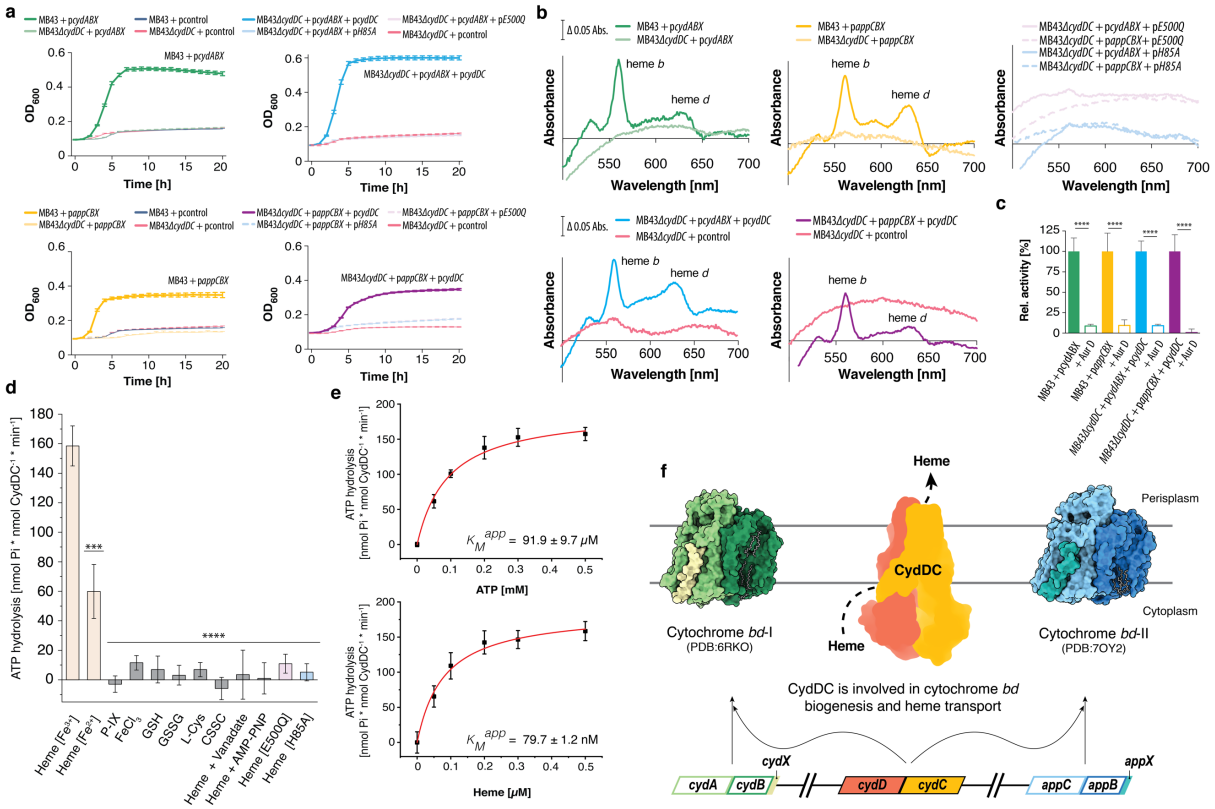

Fig. 1 – Physiological and biochemical links between CydDC activity and cytochrome *bd* biogenesis. (a) Growth complementation studies using *E. coli* MB43 and *MB43ΔcydDC*. Both strains lack NADH dehydrogenase I and all terminal oxidases. Cytochrome *bd* variants: p*cydABX* – wild-type cyt. *bd*-I; p*appCBX* – wild-type cyt. *bd*-II. CydDC variants: p*cydDC* – wild-type variant; p*E500Q* - glutamate to glutamine exchange at position 500 of CydC; p*H85A* - histidine to alanine exchange at position 85 of CydC. Control plasmid: pcontrol - empty pET17 vector **(b)** Reduced-minus-oxidized UV-Vis spectra (450 - 700 nm) of membrane fractions from strains with restored/impaired growth phenotypes. Peaks corresponding to *b*-type and *d*-type hemes are indicated. **(c)** Oxygen reductase activity of membranes from strains with growth-active phenotypes following complementation with structural genes of cytochrome *bd*-I, *bd*-II, and CydDC, respectively. Aurachin D (Aur. D) induced inhibition of oxygen consumption indicates for cytochrome *bd* specific oxygen reductase activity. Data are given as mean of n=3 ± SD. Significance was assessed based on a paired two-tailed Student's t-test (**** $p < 0.0001$). **(d)** ATP hydrolysis activity of CydDC in the presence of putative substrate molecules. Data are given as mean of n=3 ± SD. Significance was assessed based on a paired two-tailed Student's t-test (***, $p < 0.001$; ****, $p < 0.0001$). **(e)** Titration experiments for the determination of Michaelis constants (K_M^{app}) for ATP (91.9 ± 9.7 μM) and heme (79.7 ± 1.2 nM). All presented ATP hydrolysis data are corrected for background activity in the absence of substrate candidates. **(f)** Working model for substrate specificity and physiological role of CydDC based on independent physiological and biochemical data generated in this study.

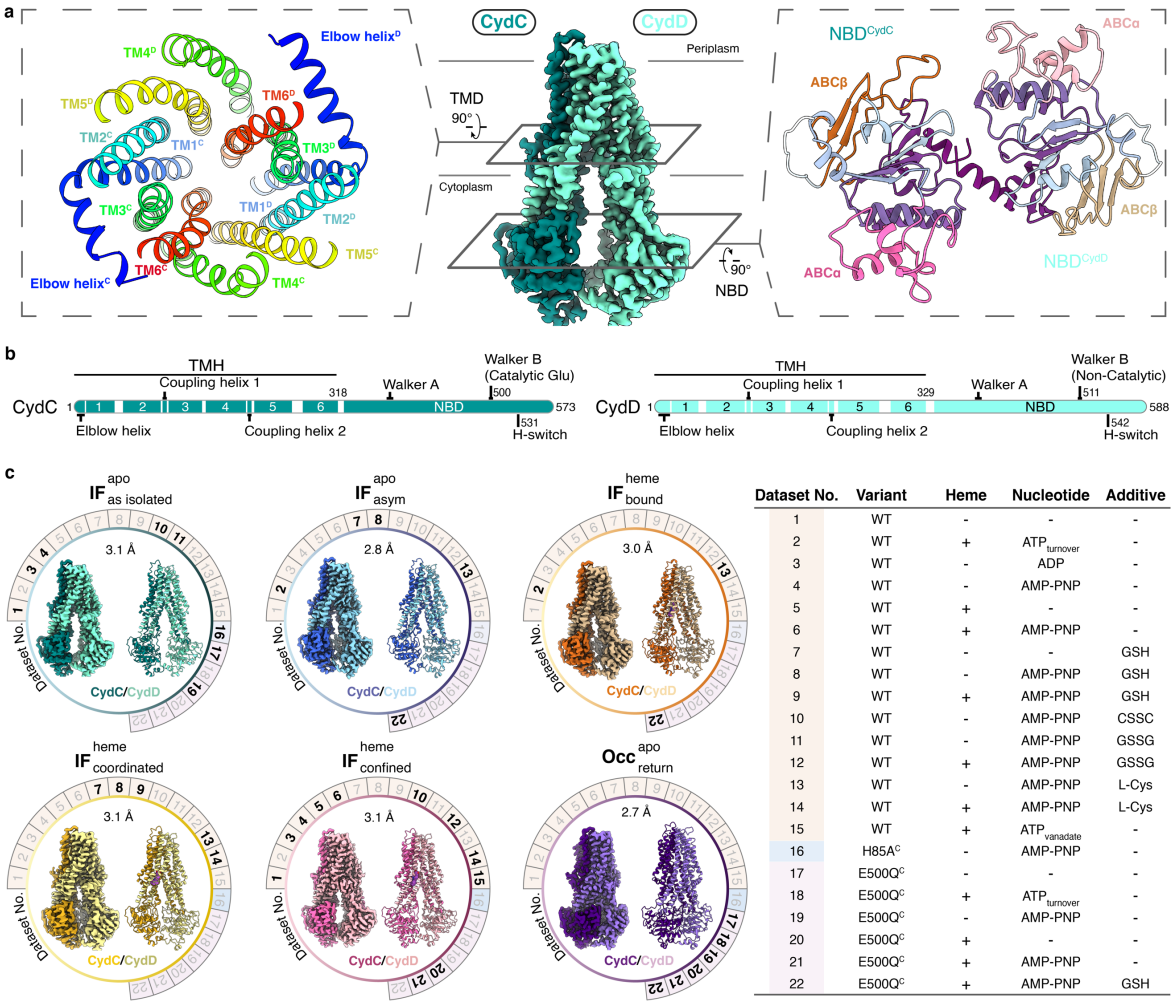

Dataset No.	Variant	Heme	Nucleotide	Additive
1	WT	-	-	-
2	WT	+	$ATP_{turnover}$	-
3	WT	-	ADP	-
4	WT	-	AMP-PNP	-
5	WT	+	-	-
6	WT	+	AMP-PNP	-
7	WT	-	-	GSH
8	WT	-	AMP-PNP	GSH
9	WT	+	AMP-PNP	GSH
10	WT	-	AMP-PNP	CSSC
11	WT	-	AMP-PNP	GSSG
12	WT	+	AMP-PNP	GSSG
13	WT	-	AMP-PNP	L-Cys
14	WT	+	AMP-PNP	L-Cys
15	WT	+	$ATP_{vanadate}$	-
16	H85A^C	-	AMP-PNP	-
17	E500Q^C	-	-	-
18	E500Q^C	+	$ATP_{turnover}$	-
19	E500Q^C	-	AMP-PNP	-
20	E500Q^C	+	-	-
21	E500Q^C	+	AMP-PNP	-
22	E500Q^C	+	AMP-PNP	GSH

Fig. 2 – Systematic cryo-EM approach. (a) Volume map representation of the overall CydDC structure. Dark green, CydC; light green, CydD. Left: cross-section of the membrane domain composed of 12 TMs showing arrangement and geometry typical for type IV ABC transporters. Right: cross-section of nucleotide-binding domains (NBDs). The subdomains ABCα and ABCβ of each NBD are highlighted. ATP-binding sites are indicated by dashed circles. **(b)** Schematic organization of CydC and CydD subunits. TMs are indicated by numbers. Residues important for ATP hydrolysis and signal transduction between TMH and NB domains are highlighted. **(c)** Summary of systematic single-particle cryo-EM studies. Left: volume maps and corresponding ribbon models within each circle represent a distinct conformation of CydDC. Numbers around circles refer to sample condition of CydDC analyzed by electron microscopy. Bold numbers indicate that the given conformation was present under that condition. Right: summarized information about the analyzed CydDC variants, presence and absence of heme, nucleotide, and additional putative substrate molecules. CydDC^{wt}, beige; CydDC^{H85A}, light blue; CydDC^{E500Q}, purple. IF, inward-facing; Occ, occluded.

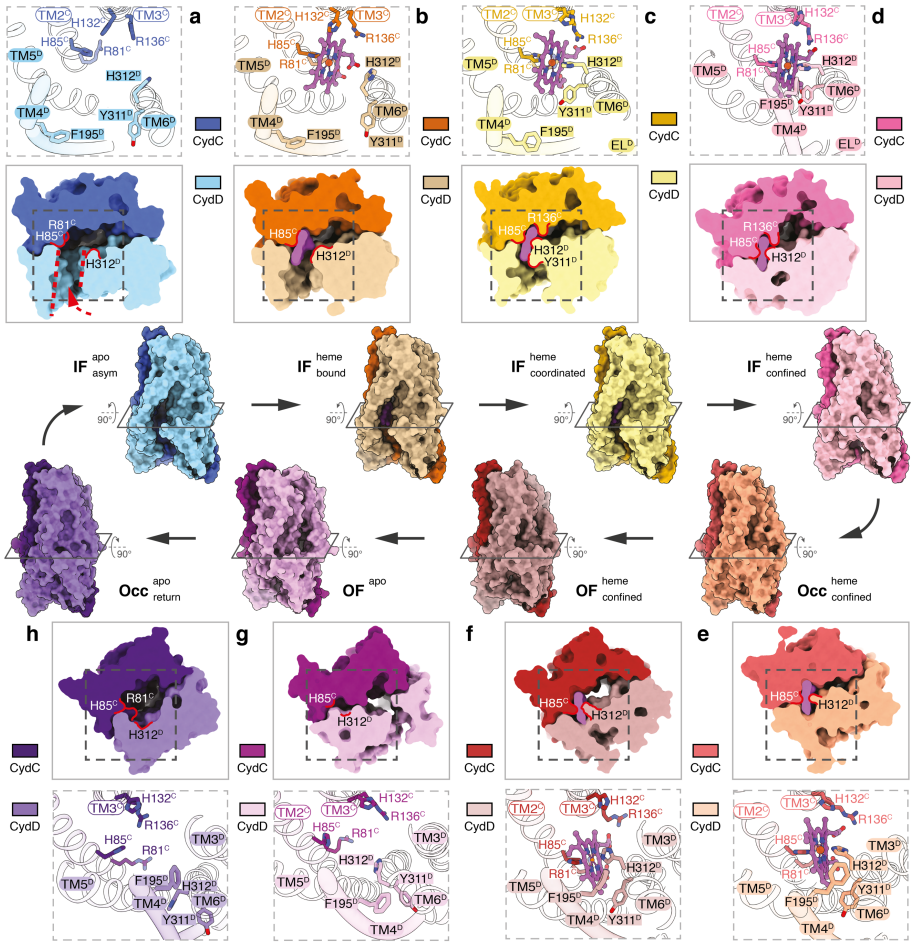

Fig. 3 – Conformational landscape of heme binding and translocation. Closeup views show residues involved in heme binding and occlusion. Surface model cross sections illustrate the changing shape and size of the internal cavity in different conformational states. Surface model side views highlight the change in overall shape of the TMH region in different conformational states. Heme is shown as purple ball and stick model. EL1^{D} and TM4^{D} are shown as tubes. Models **a-d** and **h** refer to cryo-EM structures. Models **e-g** were built computationally by MD simulations. IF, inward-facing; OF, outward-facing; Occ, occluded.

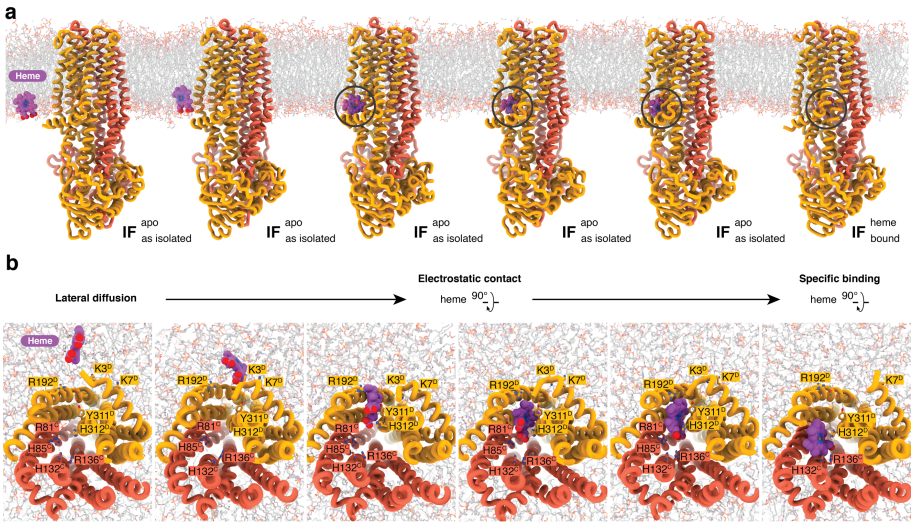

Fig. 4 – Structural dynamics of the heme binding and flipping mechanism. (a) Representative snapshots of MD simulations showing the lateral diffusion and entry of heme to the membrane-accessible binding cavity of CydDC. **(b)** Closeup views show that once heme interacts with the electrostatic surface and the interior of the binding cavity of CydDC, a 90° rotation occurs that orients the propionate groups of the porphyrin macrocycle horizontally. A second 90° rotation takes place upon bilateral axial coordination via H85^{C} and H312^{D}, which results in a complete flip of the heme molecule compared to its conformation when immersed freely within the lipid bilayer.

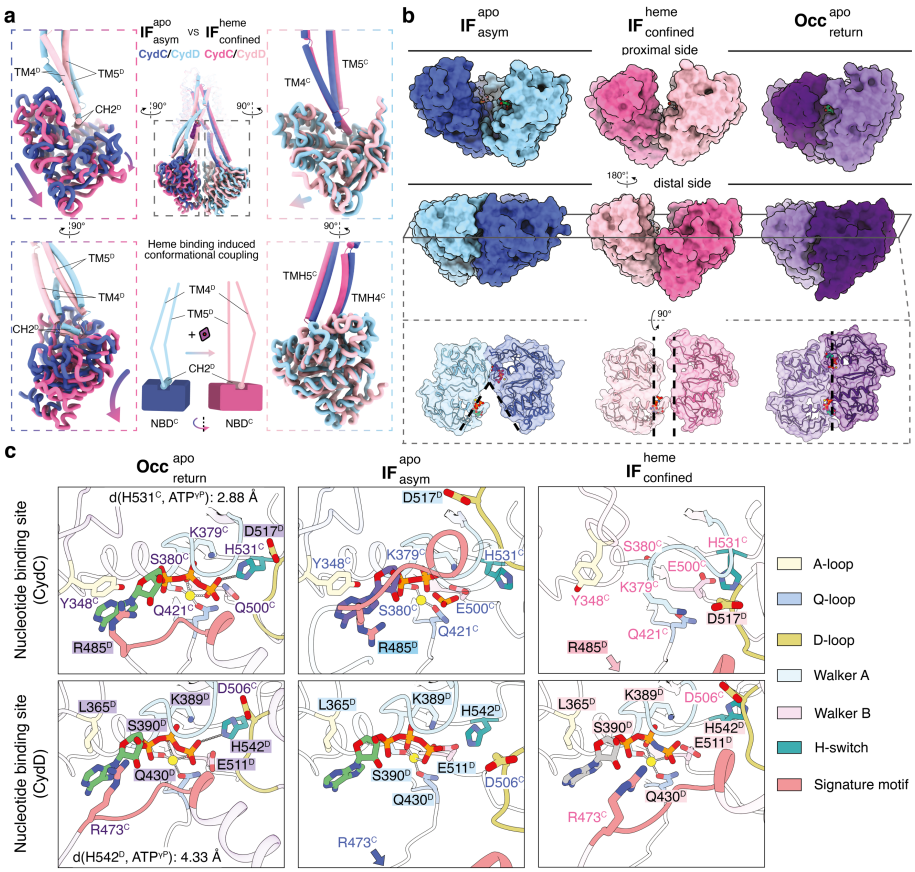

Fig. 5 – Signal transduction between TMH and NB domains. (a) Mechanism of conformational coupling between TMH and NB domains. Occlusion of the lateral substrate gate induces conformational changes of TMs 4 & 5 of CydD causing a rotational movement of NBD^C via coupling helix 2 ($CH2^D$). No conformational coupling between TMs of CydC and NBD^D is observable. Dark blue, CydC; light blue, CydD; dark pink, CydC; light pink, CydD. **(b)** Surface representation of NBD-NBD interactions in proximal and distal view. Cross section top view on the level of the nucleotide-binding sites (NBS) shows distinctly different NBD conformations. $\mathbf{IF}^{\mathrm{apo}}_{\mathrm{asym}}$, blue; $\mathbf{IF}^{\mathrm{heme}}_{\mathrm{confined}}$, magenta; $\mathbf{Occ}^{\mathrm{apo}}_{\mathrm{return}}$, purple. **(c)** Closeup view of nucleotide-binding pockets in different conformational states and nucleotide occupancies. Conserved structural motifs of the nucleotide-binding and hydrolysis sites are highlighted. ATP, green; ADP, purple; AMP-PNP, grey; phosphate, orange; Mg^{2+}, yellow.

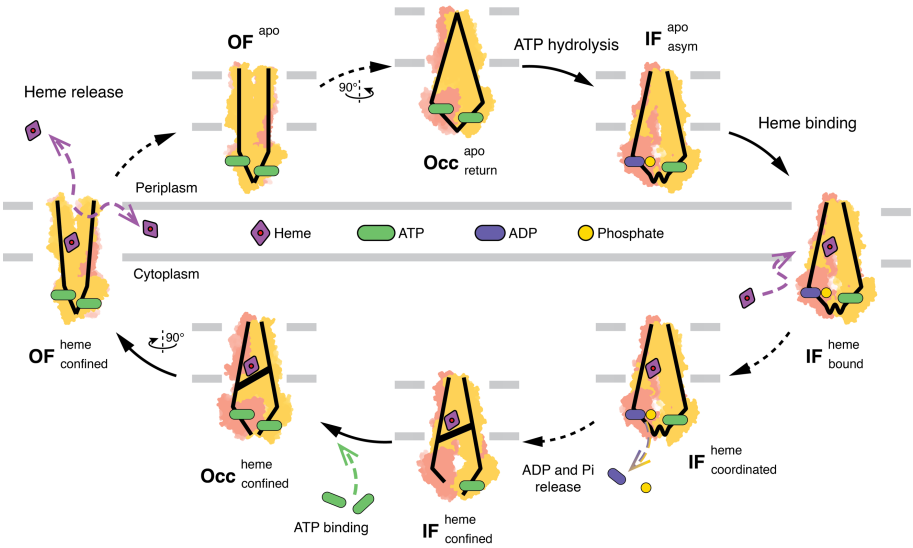

Fig. 6 – Schematic model of heme transport facilitated by CydDC. Energy of ATP hydrolysis at NBD^{C} converts CydDC from the $\mathbf{Occ}^{\mathrm{apo}}_{\mathrm{return}}$ state to the $\mathbf{IF}^{\mathrm{apo}}_{\mathrm{asym}}$ state. Binding of heme to its dedicated pocket causes closing of the lateral substrate gate and triggers the release of ADP + Pi caused by conformational changes of the nucleotide-binding site of CydC. Transport of heme does occur independent of ATP hydrolysis but requires binding of ATP. Separation of TM lobes and rearrangement of residues around the heme-binding pocket cause the release of heme either towards the periplasmic space or to the periplasmic bilayer leaflet of the membrane.